SAND2020-4497C
Proceedings of the ASME 2020 Pressure Vessels & Piping Conference
PVP 2020
July 19-24, 2020, Minneapolis, MN, USA

PVP2020-8576

HYDROGEN EFFECTS ON FATIGUE LIFE OF WELDED AUSTENITIC STAINLESS STEELS EVALUATED WITH HOLE-DRILLED TUBULAR SPECIMENS

B. Kagay, C. San Marchi, V. Pericoli, J. Foulk III
Sandia National Laboratories
Livermore, CA, USA

ABSTRACT

Limited fatigue data exists for small-volume welded austenitic stainless steel components typically employed in hydrogen infrastructure due to the difficulty of testing these components with conventional specimen designs. To assess the fatigue performance of orbital tube welds of austenitic stainless steels, a hole-drilled tubular specimen was designed to produce a stress concentration in the center of the orbital weld. Fatigue life testing was performed on welded and non-welded 316L stainless steel hole-drilled tubular specimens, and the effects of hydrogen were evaluated by testing specimens with no added hydrogen and with internal hydrogen introduced through gaseous precharging. When accounting for the differences in flow stress caused by microstructural variations and the presence of internal hydrogen, the total fatigue life and fatigue crack initiation life of the welded and non-welded tubes were comparable and were reduced by internal hydrogen. In addition, the fatigue life results produced with the hole drilled tubular specimens were consistent with fatigue life data from circumferentially notched stainless steel specimens that have a similar elastic stress concentration factor. To better understand the mechanics of this specimen geometry, mechanics modeling was performed to compare the stress and strain distributions that develop at the stress concentration in the hole-drilled tubular and circumferentially notched specimens during fatigue cycling.

INTRODUCTION

Components in pressurized hydrogen systems are commonly produced from austenitic stainless steels, such as type 316 and type 316L. When integrating components into a pressure system, welding is preferred to minimize leaks associated with compression fittings. Studies have shown the tensile ductility of austenitic stainless steels with a high nickel content to be negligibly affected by both gaseous external hydrogen [1, 2], and internal hydrogen introduced by thermal gaseous pre-charging [1, 3], which has resulted in the perception that these steels are generally immune to hydrogen induced failures. However, there also exists a concern that austenitic stainless steel welds may be more embrittled in hydrogen environments than the base metals due to variations in the microstructure of the welds. Several studies have shown that austenitic stainless steel welds tensile tested with internal hydrogen exhibit comparable ductility to that of the base metals (reduction of area (RA) > 40%)) [4–6]; however, variations in welding methodology have been shown to produce microstructural features that increase the susceptibility of welds to hydrogen cracking in fracture tests [4-6]. Specifically, greater δ ferrite content and long dendritic features (especially when aligned parallel to the crack propagation direction) have been associated with degradation of fracture toughness of austenitic stainless steels with internal hydrogen [5, 6].

Assessment of fatigue performance is also necessary for alloy selection and design of high-pressure hydrogen pressure systems, such as hydrogen refueling stations. In general, tensile results are insufficient to assess fatigue resistance in gaseous hydrogen environments. A decrease in fatigue life for austenitic stainless steels when tested in external gaseous hydrogen has been observed [7, 8]. For several austenitic alloys tested in external hydrogen, the applied stress versus cycles to failure curves (S-N curves) were observed to superimpose when the applied fatigue stress was normalized by the ultimate true tensile stress [9]. Crack initiation life measured for these alloys through the direct current potential difference (DCPD) technique also superimposed with the same normalization, indicating similar crack initiation and growth behaviors [9]. S-N curves from testing of austenitic stainless steels with internal hydrogen closely represent the data from testing in external hydrogen when the applied fatigue stresses are normalized by the yield or tensile stresses to account for the strengthening associated with internal hydrogen [7, 10].

In this study, the effects of hydrogen on the fatigue performance of 316L stainless steel orbital tube welds and non-welded tubes are compared through load-controlled fatigue testing of hole-drilled tubular specimens with and without internal precharged hydrogen. The DCPD technique is used to evaluate fatigue crack initiation life, as well. The influence of

Sandia National Laboratories is a multimission laboratory managed and operated by National Technology & Engineering Solutions of Sandia, LLC, a wholly owned subsidiary of Honeywell International Inc., for the U.S. Department of Energy's National Nuclear Security Administration under contract DE-NA0003525.

specimen configuration on fatigue life is assessed through comparison with results generated from previous testing of circumferentially notched tensile (CNT) specimens and solid mechanics simulation.

EXPERIMENTAL PROCEDURES

Commercially-available 316L stainless steel tubing with the composition provided in Table 1 was evaluated. The tubing had a nominal outer diameter of 6.35 mm and a nominal inner diameter of 3.81 mm. Tubing was sectioned into 100 mm long lengths to produce non-welded tube specimens. Orbital tube weld specimens were produced through single pass, gas tungsten arc welding of two pieces of 50 mm long tubing with automated commercial orbital tube welding equipment. Tensile testing was performed with these welded and non-welded specimens. For fatigue testing, a hole with a diameter of 1.78 mm was drilled at the midpoint of the specimens and through both walls to produce a stress concentrator with K_t of 3. The holes were drilled in the welded specimens so that the midpoint of the hole corresponded to the center of the weld. The composition of a 316L bar material is also provided in Table 1 and represents the material from which CNT specimens were manufactured in a previous study [7]. The CNT specimens possess a K_t of 3.9.

Tensile testing of tube specimens with no holes was performed with an engineering strain rate of 0.02 s^{-1} and with a 25 mm (1.0 in) extensometer to measure elongation. The same servohydraulic load frame was used for all tensile and fatigue tests. For tensile and fatigue testing, 25 mm long pins were inserted into the top and bottom ends of the specimens, and the specimens were clamped with wedge grips over the regions with the pins resulting in a length between the grips of approximately 50 mm.

Load-control tension-tension fatigue testing was performed with an R-ratio of 0.1 and a frequency of 1 Hz. The nominal applied net section stresses were calculated based on the applied load and the minimum initial cross-sectional area, which is the initial cross-sectional area of the specimen at the center of the hole. Fatigue testing was performed on specimens without internal hydrogen (as-received (AR)) and with internal hydrogen (H-precharged (PC)) in the ambient laboratory environment (temperature of approximately 20°C). A uniform saturation of internal hydrogen was achieved through thermal precharging in gaseous hydrogen at a pressure of 138 MPa and a temperature of 300°C for at least 10 days. These precharging parameters result in a hydrogen concentration of approximately 140 wt. ppm [3]. After precharging the specimens were stored in a freezer at −50°C (223K) until testing to prevent hydrogen egress. The fracture surfaces produced with fatigue testing were imaged with a confocal microscope.

To measure crack initiation, the DCPD method was applied to every fatigue test. A constant current of 1 A was applied across the length of the specimen through two wires spot-welded about 40 mm away from the hole on either end of the specimen and rotated 180° from each other. Voltage measurement leads were welded across at least one of the holes of each specimen. To improve the sensitivity of the DCPD technique for these specimens, additional probes were placed at varying locations on the specimen, including across the hole on the opposite side, along the sides of the specimens, and/or very close to the edge of the hole. To minimize thermoelectric effects the direction of current flow was periodically reversed, and the time between reversals was between 5 and 25 s depending on the anticipated duration of the test. The number of cycles to crack initiation was selected as the inflection point at which the DCPD voltage signal began to continuously increase.

RESULTS

The tensile properties of the 316L tubes (316L T) and 316L welded tubes (316L WT) in the as-received (AR) and hydrogen precharged (PC) states are provided in Table 2 (tensile properties were evaluated without the hole) [4, 11]. The 316L (non-welded) tubes exhibited both a higher yield stress and ultimate engineering tensile stress (UTS) in the AR and PC conditions than the 316L welded tubes. The uniform and total elongation of the non-welded tubes was also significantly greater than the welded tubes, which is due to localization of plastic deformation in the weld compared to uniform plastic deformation across the gauge region of the non-welded tubes. Pre-charged hydrogen increased the yield stress and UTS and decreased the reduction of area (RA) of both the tubes and the welded tubes. Notably, H-precharging caused an increase in elongation for the non-welded tubes, whereas the effect of hydrogen on elongation (and ductility) of the welded tubing was mixed as reported in Ref. [11]. Weld process A from Ref.[11] was used in this study and is reported in Table 2. The tensile properties of the 316L bar material (from which circumferentially notched tensile specimens were previously tested in fatigue) are also included in Table 2 [7]. The bar material was tested in the strain-hardened condition; thus, the strength properties of the bar was nearly double the strength of the tube for both AR and PC conditions. Hydrogen precharging increased the strength properties and decreased the RA of the 316L bar material.

Table 1 – Composition of 316L Tubing and 316L Bar

wt %	Cr	Ni	Mn	Mo	C	N	Si	S	P	Cu	Fe
316L Tube	16.87	12.42	1.71	2.08	0.018	-	0.39	0.006	0.027	0.23	Bal.
316L Bar	17.54	12.04	1.15	2.05	0.02	0.04	0.51	0.023	0.028	-	Bal.

Table 2 – Tensile Properties of As-Received (AR) and Hydrogen Pre-Charged (PC) 316L Tubes (316L T), 316L Welded Tubes (316L WT), and 316L Bar

	Condition	0.2% Yield Stress (MPa)	UTS (MPa)	Uniform Elongation (%)	Total Elongation (%)	Reduction of Area (%)	Reference
316L T	AR	286	591	50	62	70	[4, 11]
316L T	PC	327	635	55	64	64	[11]
316L WT	AR	243	539	29	32	74	[11]
316L WT	PC	291	581	31	33	63	[11]
316L Bar	AR	573	731	26.6	54.5	76.6	[7]
316L Bar	PC	648	793	27.1	47.6	60.2	[7]

Fatigue life results for the tubes and welded tubes in the AR and PC conditions are plotted as maximum stress (S_{max}) versus cycles to failure in Figure 1 (a). According to the S-N curves in Figure 1 (a), the non-welded tubes exhibit greater fatigue life than the welded tubes in both the AR and PC conditions. Additionally, there is no distinguishable difference in fatigue life between the AR and PC conditions for either the tubes or welded tubes in Figure 1 (a). In general, higher strength materials exhibit greater fatigue life for a given applied stress and this is evident in the S-N curves in Figure 1 (a) where the higher strength tubes exhibit greater fatigue life than the lower strength welded tubes.

Normalization of the applied stresses by a strength parameter (yield strength, UTS, etc.) provides a means to account for the difference in strength between microstructures, as well as correct for the increase in flow strength due to internal hydrogen. More specifically, normalization by a strength parameter can account for the influence of the material properties (yield strength, strain hardening) on the evolution of the stress and strain fields during fatigue [12–14]. The engineering UTS was chosen for normalization of the maximum stresses in this study because the UTS includes contributions from both the material's yield stress and strain hardening behavior (unlike the yield stress alone), and the ultimate true tensile stress could not be reliably calculated due to uncertainty regarding the uniform elongation measurements of the welded tubes.

In Figure 1 (b), the data from Figure 1 (a) is plotted with the maximum applied stress normalized by the ultimate engineering tensile stress (S_{MAX}/UTS). When the maximum stress is normalized by the UTS, the tubes and welded tubes in the AR condition exhibit similar fatigue life. Similarly, the tubes and welded tubes in the PC condition exhibit consistent fatigue life for the same normalized stress. The fatigue life of the PC condition, however, is slightly lower than for the AR condition when the maximum stress is normalized by the UTS.

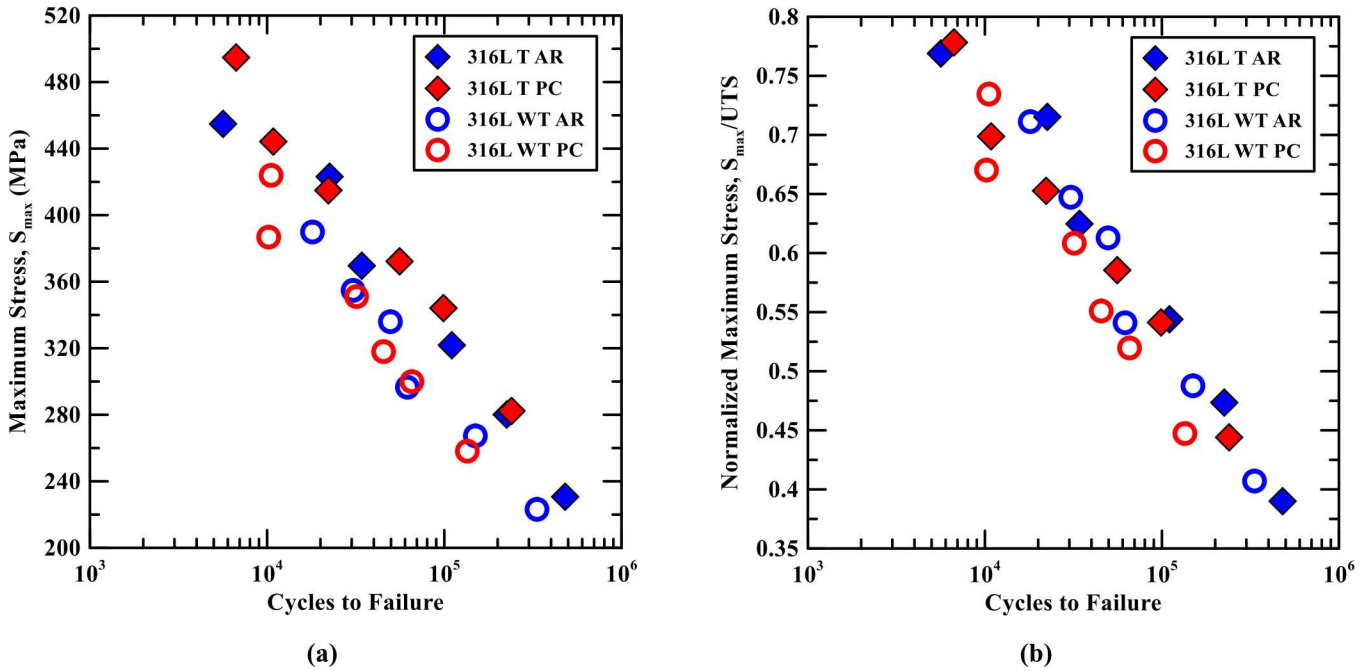

Figure 1 Fatigue life of the 316L tubes (316L T) and welded tubes (316L WT) in the AR and PC conditions plotted versus (a) maximum applied stress and (b) maximum applied stress normalized by the ultimate tensile stress (S_{max}/UTS).

The fatigue life of strain-hardened 316L bar from ref. [7] is plotted in Figure 2 (a) along with the fatigue life data from Figure 1 (b). In Figure 2 (a), the S-N curves for the 316L bar (using the CNT configuration) correspond to the S-N curves for the welded and non-welded tubes in the same (AR and PC) conditions.

The cycles to crack initiation as measured by the DCPD method are plotted versus the normalized maximum applied stress (S_{max}/UTS) for the tubes, welded tubes, and bar in the AR and PC conditions in Figure 2 (b). The same general trends are evident for cycles to crack initiation in Figure 2 (b) as for cycles to failure in Figure 2 (a): no difference in cycles to crack initiation for the tubes, welded tubes, and bar and a decrease in cycles to crack initiation for the PC conditions compared to the AR conditions. The percentage of cycles to failure necessary to initiate a crack (Percent to N_i) was calculated for each test. The average and standard deviation of the AR and PC tests, respectively, are provided in Table 3, along with the average and standard deviation considering both AR and PC results as a single data set. The average, maximum, and minimum percent of cycles to crack initiation were nearly identical for the AR and PC conditions.

Fatigue cracks in the tube and welded tube specimens all initiated at the mid-plane of the hole where the stress concentration is greatest and propagated perpendicular to the loading axis. The length of the cracks emanating from the holes prior to overload failure, however, varied from test to test. Fractographs are shown for the welded tube in the PC condition in Figure 3 (a) (S_{max} = 270 MPa) and for the non-welded tube in the AR condition in Figure 3 (b) (S_{max} = 230 MPa) and Figure 3 (c) (S_{max} = 370 MPa). In the fractographs, the overload failure is distinguished by thinning of the wall of the tube, whereas crack extension due to fatigue is represented by the uniform, maximum wall thickness (and lighter color in the fractographs). From Figure 3, it is evident that fatigue cracks could initiate and grow in several different configurations: two primary cracks emanating from one hole (Figure 3 (a)), two primary cracks propagating from both holes on one side of the specimen (Figure 3 (b)), and 4 cracks of varying length emanating from both holes on both sides of the specimen (Figure 3 (c)). The formation of two primary cracks (Figure 3 (a) and (b)) was more likely to occur for lower applied cyclic stresses, while the extension of four cracks (Figure 3 (c)) was more likely to occur for higher applied cyclic stresses. The welded tubes exhibited coarser fracture features in the fatigue cracking regions than the non-welded tubes, but the appearance of fatigue fracture features (for both the tubes and welded tubes) was not changed by precharged internal hydrogen at magnifications up to 500X.

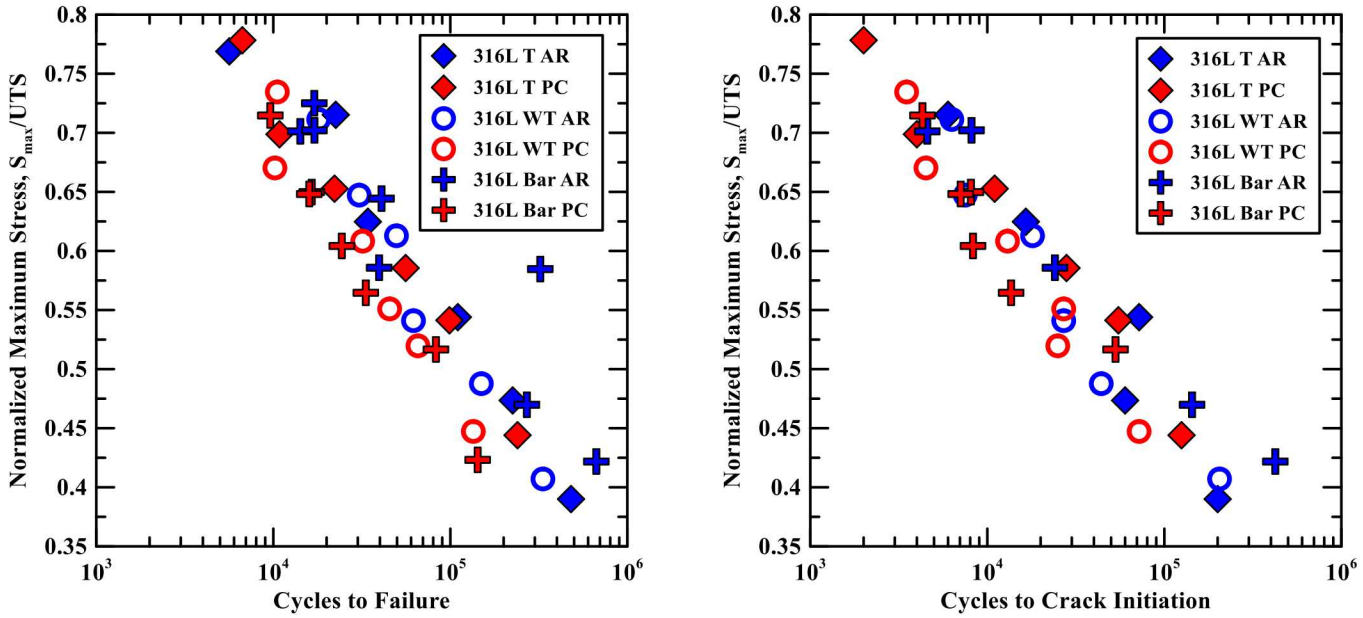

Figure 2 Maximum applied stress normalized by the ultimate tensile stress (S_{max}/UTS).versus (a) cycles to failure and (b) cycles to crack initiation for the 316L tubes (316L T), 316L welded tubes (316L WT) and 316L Bar in the AR and PC conditions. Data for 316L Bar was produced with CNT specimens [7].

Table 3 – Average, Standard Deviation, Maximum and Minimum Percentage of Cycles to Failure Prior to Crack Initiation (Percent to N_i) of AR and PC Conditions for all Materials (316L T, 316L WT, 316L Bar).

Condition	Average Percent to N_i	St. Dev. Percent to N_i	Maximum Percent to N_i	Minimum Percent to N_i
AR	43.5	14.2	65.3	24.5
PC	45.6	9.4	63.9	29.9
AR+PC	44.6	11.7	65.3	24.5

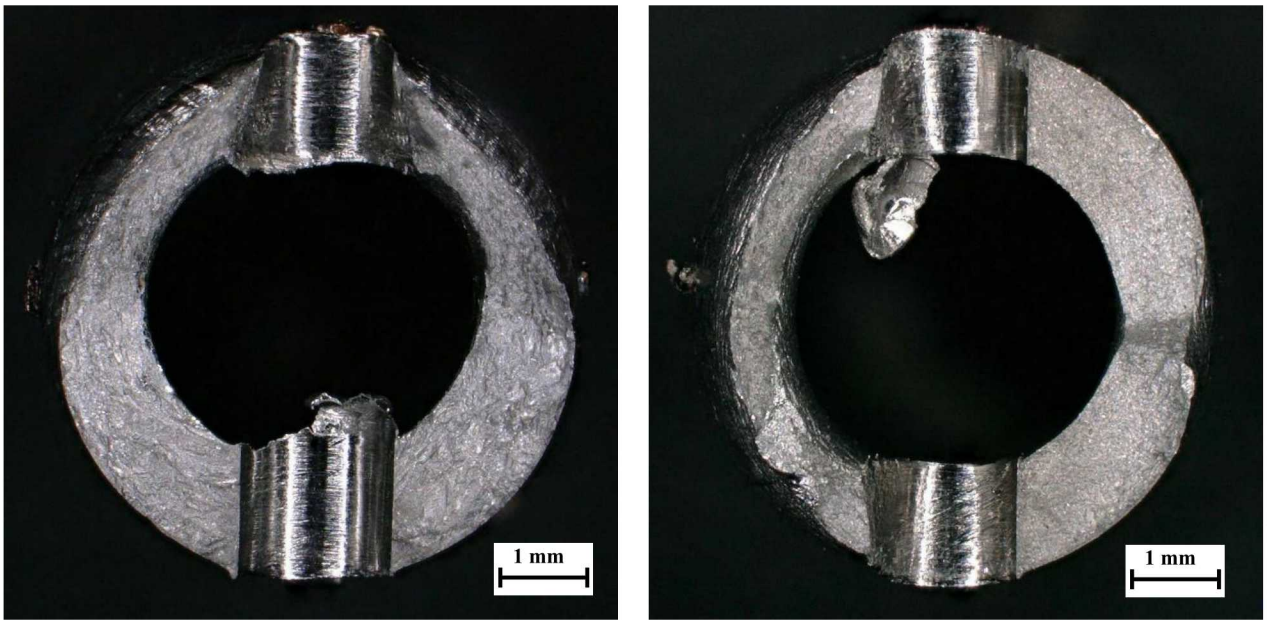

(a) **(b)**

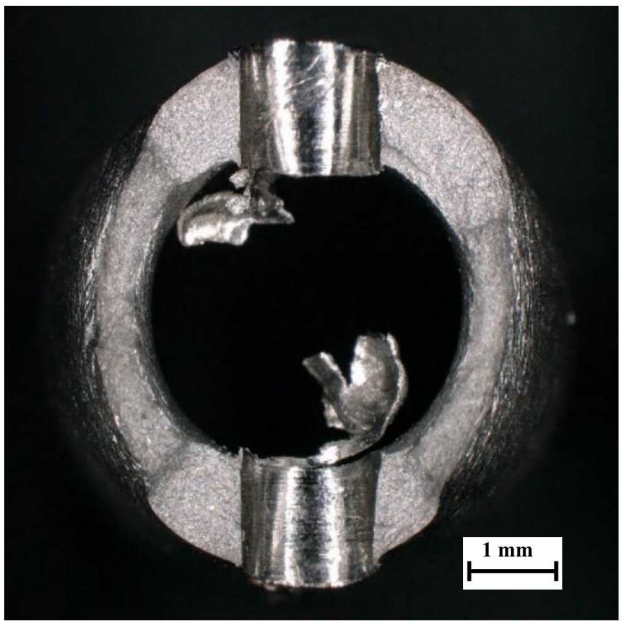

(c)

Figure 3 Fractographs of (a) 316L WT PC with S_{max}= 270 MPa, (b) 316L T AR with S_{max}= 230 MPa, and (c) 316L T AR with S_{max}= 370 MPa.

MODELING

To better understand the mechanistic response of both circumferentially notched (CNT) and tube specimens, finite element modeling was employed for representative loading. Whereas the materials were different for the tube, weld and bar, for the purposes of the modeling, the constitutive response was assumed to be the same. As previously mentioned, the elastic stress concentration for both specimen geometries is quite similar. Our goal, however, is to consider inelasticity and the impact of specimen constraint on evolving fields. All quasi-static analysis accounting for finite deformations was performed using Sierra/SM [15].

The local discretizations for each specimen are illustrated in Figure 4. The models consider symmetry for computational efficiency. The CNT geometry is represented as an axisymmetric, 10 degree wedge, while the tube geometry is represented by a $1/8^{th}$ model. Both models employ high-order 10-noded composite tetrahedral elements, with a constant pressure formulation to alleviate volumetric locking for isochoric, plastic deformations [16]. The mesh discretizations were sufficient to resolve the local plastic deformations at the respective stress concentrations; the element size near the stress concentrator is approximately 7 microns in the CNT specimen and 25 microns in the tube specimen. Far-field traction is applied such that the net-section traction for both geometries is 500 MPa. Initial findings focus on capturing the flow characteristics of the 316L tubes. The same constitutive model and parameters were employed for both geometries. Although we will incorporate aspects of the backstress in future work, initial efforts employed a rate-independent, user-defined, isotropic hardening model. The functional form of the flow curve (Equation 1) incorporates hardening and recovery transients to adequately resolve the initial knee and subsequent large-deformation hardening of 316L.

$$\bar{\sigma} = \sigma_Y + \frac{H}{R_d}\left[1 - \exp\left(-R_d \bar{\varepsilon}_p\right)\right] + H_L \bar{\varepsilon}_p \qquad (1)$$

Figure 5 illustrates the fit of experimental data under monotonic uniaxial tension for the strain-hardened 316L bar. Parameters for the yield strength (σ_Y), linear hardening (H_L), and hardening and recovery terms (H, R_d) are 495 MPa, 1025 MPa, 40.16 GPa, and 222, respectively. Because we are focused on inelasticity in the small-strain regime, we emphasize that the model yield strength represents the departure from linearity.

In an effort to consider similitude in the first few cycles, both geometries were simulated to ten cycles with roughly 200 time steps per cycle to resolve history-dependent behavior. Consistent L_2 projections of integration point quantities result in continuous, global fields. We extract those fields ahead of the notch tips for comparison. Because the CNT is axisymmetric, only one curve is extracted. For the tube geometry, fields are sampled at the inner, mid, and outer radius in the circumferential direction. Figures 6 through 9 illustrate the triaxiality, Mises stress, equivalent plastic strain, and the local R-ratio for both geometries. For readability, we normalize the Mises stress by the initial yield stress. To focus on the near-field, quantities are plotted over length scales in which the CNT sample is plastically deforming (i.e. exhibits nonzero equivalent plastic strain), about 0.14 mm.

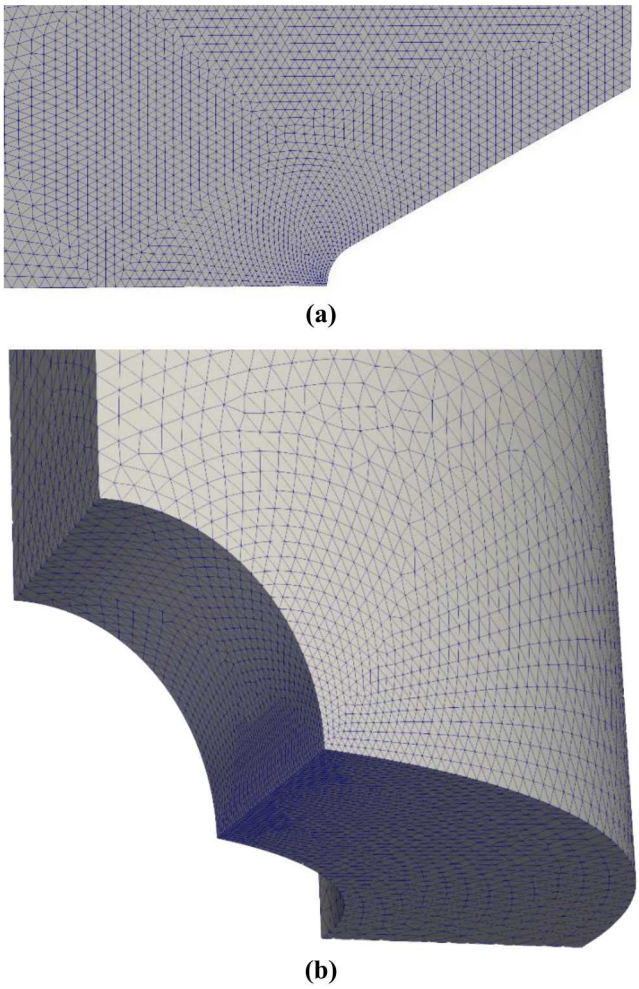

(a)

(b)

Figure 4 Local mesh discretization of (a) the CNT specimen, and (b) the tube specimen.

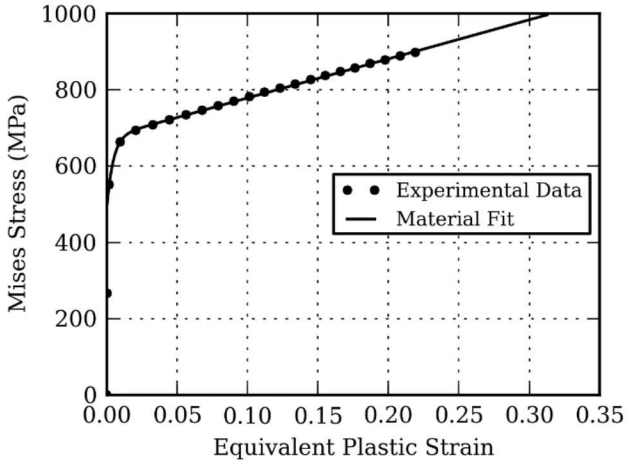

Figure 5 Constitutive material fit under monotonic uniaxial tension.

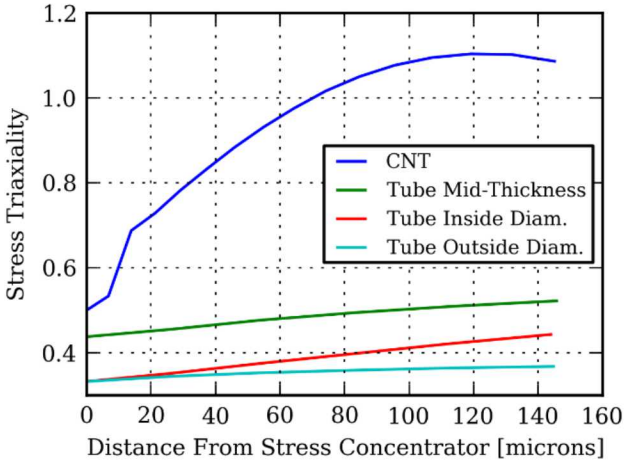

Figure 6 Local stress triaxiality near the stress concentrator at cycle 10.

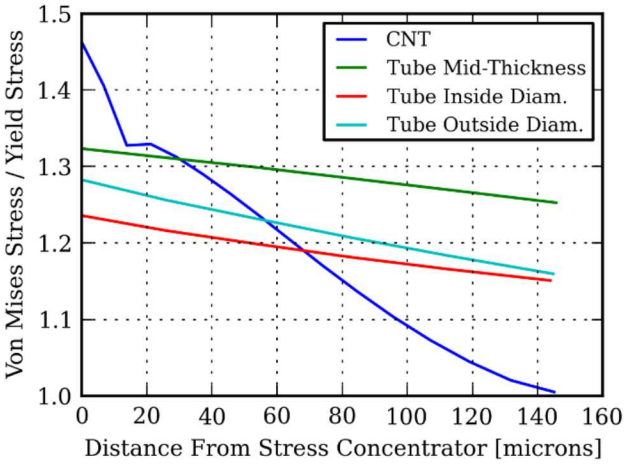

Figure 7 Local von Mises stress normalized by the yield stress near the stress concentrator at cycle 10.

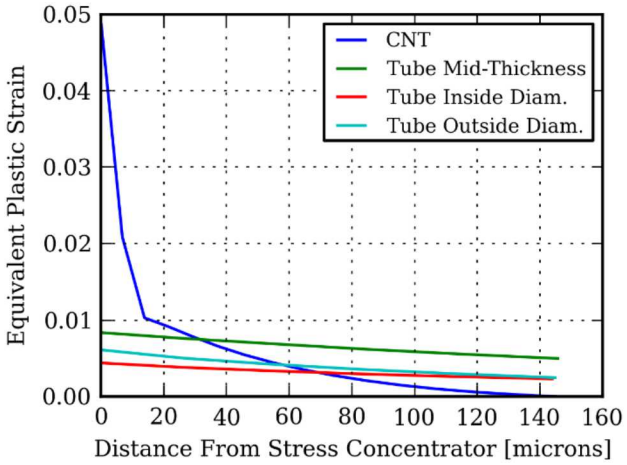

Figure 8 Local equivalent plastic strain near the stress concentrator at cycle 10.

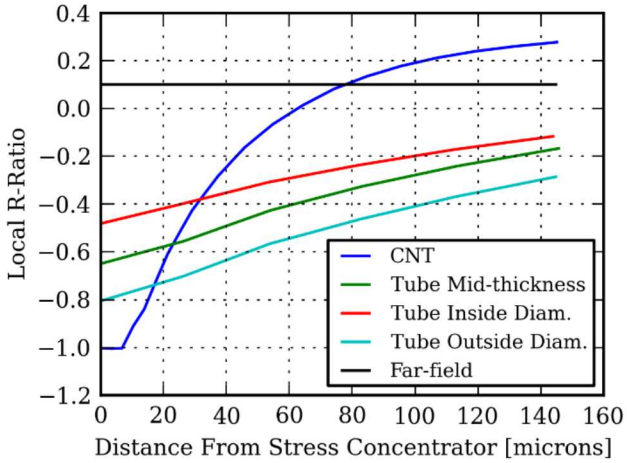

Figure 9 Local R-ratio near the stress concentrator at cycle 10.

Whereas the elastic stress concentration is similar, the hole-drilled tube and CNT geometries differ in both in-plane and through-thickness constraint. The triaxiality clearly illustrates those differences. Along the axial mid-plane of the geometries, the plastic zone for the CNT and tube geometry is on the order of 0.140 mm and 1.2 mm, respectively. Interestingly, although the character of the outer plastic zone might be described as contained and widespread, the two geometries overlap in the Mises stress and the equivalent plastic strain over a near-field region spanning 20 µm to 80 µm. A local, spatially varying R-ratio derived from the axial stress is also constructed to aid the reader (Figure 9). Although this quantity is cycle dependent, we initially construct the quantity based on both the maximum and minimum for all cycles with $R_{local} = \min(\sigma_{axial,local})/\max(\sigma_{axial,local})$. Due to the stress concentration, the CNT geometry yields fully-reversed loading near the notch tip. In contrast, the tube has less constraint and more diffuse plasticity, resulting in less local compression near the transverse hole and smaller magnitude of reverse loading. Local R-ratios in the tube, however, are still negative, substantial, and deviate from the far-field, imposed R-ratio of 0.1. Like quantities that reflect the deviatoric response, local R-ratios overlap in the aforementioned near-field region around 25 µm. In fact, the overlap in the local R-ratio which stems from the axial stress does reflect potential similarities in the elastic response. Near-field elasticity provides the constraint for compressive stresses which result in local, negative R-ratios. More quantities will be explored as we increase model complexity, but initial findings indicate that although the gradients of field quantities are dissimilar due to differing constraint, the mean character is comparable between 20 µm to 80 µm. Future work will consider this mean behavior which stems from dissimilar gradients in the context of nonlocality and/or statistical sampling.

DISCUSSION

The measured fatigue life and number of cycles to crack initiation depend on the yield strength and strain hardening behavior of the material, as exemplified by the fatigue life curves for the tube, welded tube, and bar materials. When the applied fatigue stresses are normalized by the ultimate tensile strength, however, the fatigue life curves collapse into a narrow band, as has also been observed for several austenitic stainless steels tested in external gaseous hydrogen [9]. Seemingly, normalization of the applied fatigue stress accounts for differences in the constitutive behavior of the material. As stated elsewhere, this correspondence in fatigue life to a normalized stress parameter implies that the local stress state at the notch dictates fatigue life [9].

The solid mechanics simulations were employed to test the hypothesis that fatigue life in the presence of a stress concentration can be attributed to commonality in the local stress state. The modeling results of the CNT and tube specimens indicate an overlap in the Mises stress (Figure 7), equivalent plastic strain (Figure 8), and local R-ratio (Figure 9) fields over a distance of 20-80 μm ahead of the specimen stress concentrator. The similarity in crack initiation lives between the CNT and tube specimens suggest that the comparable mechanics of the specimens may drive crack initiation in this region ahead of the specimen stress concentrators. On the other hand, the same constitutive material model was employed for simulations of both specimen geometries, but the actual materials exhibit different tensile properties. It is unknown at this point how the fields align for dissimilar materials so further investigation of the interplay between material parameters and specimen geometry is required through both experimental and simulation methodologies. Nevertheless, while there are clear differences in the stress and strain fields ahead of the stress concentration in the hole-drilled tube and CNT specimens, the similarity of the fields for the two geometries supports the notion that crack initiation and fatigue life behavior can be captured in a general sense with baseline understanding of the solid mechanics in the presence of a stress concentration.

For the CNT specimens, a majority of the fatigue life is composed of the cycles to initiate and evolve a small crack (size of 0.15-0.30 mm) [9]. The same observation appears to be true for the hole-drilled tube specimens. Therefore, the total fatigue life for both specimens may be dominated by the cycles required to initiate and grow a crack to a critical size so that the number and final length of the cracks do not significantly affect the measured fatigue life. Indeed, crack initiation appears insensitive to the specimen geometry (hole-drilled tube versus CNT) or the microstructure (welded versus non-welded versus strain-hardened) providing additional support of the hypothesis that crack initiation and fatigue life in this class of materials can be generalized.

Fatigue crack initiation and total fatigue life are both decreased by internal hydrogen, but the ratio remained approximately the same: cycles to initiation was about 44% for the AR condition compared to 46% for the PC condition. The similarity in percentage of cycles to initiate a crack in the AR and PC conditions indicates that the micromechanisms by which internal hydrogen effects the processes for fatigue crack initiation and crack propagation may be similar.

The welded tubes also exhibited similar fatigue crack initiation and total fatigue life to the non-welded tubes and the strain-hardened bar suggesting a common response for all three microstructures (annealed tube, welded tube and strain-hardened bar). The welds tested here may exhibit similar fatigue performance in internal hydrogen to the non-weld microstructures due to a lack of microstructural features in the welds that would significantly influence hydrogen-affected fatigue crack initiation and propagation processes. Specifically, long dendritic features aligned with the crack propagation direction and a high amount of δ-ferrite are absent in these autogenous orbital tube welds, unlike the gas-tungsten arc (GTA) welds reported in ref. [5]. The low energy input in the orbital tube weld configuration compared to a conventional GTA welding process results in a finer microstructure and improved resistance to hydrogen-assisted fracture [6].

Residual stresses due to the welding process were not evaluated, but the similarity of the response of the non-welded and welded tubes implies that the residual stresses are small or dominated by the plasticity ahead of the stress concentration. The latter explanation seems the most likely as any residual stress (which is elastic by definition) will be subsumed by the plasticity that is imposed in the vicinity of the stress concentration. Indeed, plasticity at the stress concentration imposes sufficient kinematic mismatch to induce large compressive stresses upon load reversal.

The fatigue lives of welds were successfully measured through the hole-drilled tube design, which induced fatigue crack initiation and growth in the center of the welds. Fatigue of different regions of welds or the heat-affected zone could easily be evaluated by simply changing the location of the hole in the specimen. The hole-drilled tube specimens provide a method for evaluating the fatigue lives of both tubes and orbital tube welds that is consistent with other common methods of evaluating fatigue life of austenitic stainless steels (tension-tension testing of notched specimens and tension-compression testing of smooth specimens). Additionally, the hole-drilled tube configuration enables testing of relevant welds that can be readily tested in external hydrogen gas.

CONCLUSIONS

The fatigue performance of orbital tube welds of 316L austenitic stainless steel was evaluated by developing a hole-drilled tubular specimen that centers a stress concentration (and fatigue failure) in the orbital tube weld. Load-control fatigue life testing was performed on welded and non-welded hole-drilled tubular specimens both with and without internal (gaseous precharged) hydrogen. Fatigue crack initiation was determined with the DCPD method. The total fatigue life and cycles to crack initiation of the tubes and welded tubes were comparable when the applied cyclic stress was normalized by the ultimate tensile strength. Introduction of internal hydrogen into the test specimens reduced fatigue crack initiation and fatigue

life, but the ratio of initiation and life remained about the same. The fatigue life curve produced with the hole-drilled tubular specimens was consistent with fatigue life data from 316L bar in the CNT configuration when the same normalization was applied.

ACKNOWLEDGEMENTS

The authors gratefully acknowledge assistance from J.A. Campbell for hydrogen pressure systems support. We also acknowledge the funding support of the Energy Efficiency and Renewable Energy Office's Fuel Cell Technologies Office at the U.S. Department of Energy. Sandia National Laboratories is a multimission laboratory managed and operated by National Technology and Engineering Solutions of Sandia, LLC., a wholly owned subsidiary of Honeywell International, Inc., for the U.S. Department of Energy's National Nuclear Security Administration under contract DE-NA-0003525.

REFERENCES

1 C. San Marchi, T. Michler, K. A. Nibur, and B. P. Somerday, "On the physical differences between tensile testing of type 304 and 316 austenitic stainless steels with internal hydrogen and in external hydrogen," *Int. J. Hydrogen Energy*, vol. 35, no. 18, pp. 9736–9745, 2010.

2 T. Michler, Y. Lee, R. P. Gangloff, and J. Naumann, "Influence of macro segregation on hydrogen environment embrittlement of SUS 316L stainless steel," *Int. J. Hydrogen Energy*, vol. 34, no. 7, pp. 3201–3209, 2009.

3 C. San Marchi, B. P. Somerday, X. Tang, and G. H. Schiroky, "Effects of alloy composition and strain hardening on tensile fracture of hydrogen-precharged type 316 stainless steels," *Int. J. Hydrogen Energy*, vol. 33, no. 2, pp. 889–904, 2008.

4 L. A. Hughes, B. P. Somerday, D. K. Balch, and C. San Marchi, "Hydrogen compatibility of austenitic stainless steel tubing and orbital tube welds," *Int. J. Hydrogen Energy*, vol. 39, no. 35, pp. 20585–20590, 2014.

5 H. F. Jackson, K. A. Nibur, C. San Marchi, J. D. Puskar, and B. P. Somerday, "Hydrogen-assisted crack propagation in 304L/308L and 21Cr-6Ni-9Mn/308L austenitic stainless steel fusion welds," *Corros. Sci.*, vol. 60, pp. 136–144, 2012.

6 J. Ronevich, C. San Marchi, and D. K. Balch, "Evaluating the Resistance of Austenitic Stainless Steel Welds to Hydrogen Embrittlement," (PVP2019-93823), ASME Pressure Vessels and Piping Division Conference, 14-19 July 2019, San Antonio TX.

7 P. J. Gibbs, C. San Marchi, K. A. Nibur, and X. Tang, "Comparison of Internal and External Hydrogen on Fatigue-Life of Austenitic Stainless Steels," (PVP2016-63563), ASME Pressure Vessels and Piping Division Conference, 17-21 July 2016, Vancouver, Canada.

8 C. San Marchi, J. Yamabe, M. Schwarz, H. Matsunaga, S. Zickler, S. Matsuoka, and H. Kobayashi, "Global Harmonization of Fatigue Life Testing in Gaseous Hydrogen," (PVP2018-84898), ASME Pressure Vessels and Piping Division Conference, 15-20 July 2018, Prague, Czech Republic.

9 K. A. Nibur, P. J. Gibbs, J. W. Foulk, and C. San Marchi, "Notched Fatigue of Austentic Alloys in Gaseous Hydrogen," (PVP2017-65978), ASME Pressure Vessels and Piping Division Conference, 16-20 July 2017, Waikoloa, Hawaii.

10 C. San Marchi, P. Gibbs, J. Foulk, and K. Nibur, "Fatigue Life of Austenitic Stainless Steel in Hydrogen Environments," in *43rd MPA Seminar*, 2017.

11 C. San Marchi, L. A. Hughes, B. P. Somerday, and X. Tang, "Hydrogen-assisted fracture of type 316L tubing and orbital welds," in (PVP2013-97538), ASME Pressure Vessels and Piping Division Conference, 14-18 July 2013, Paris, France.

12 C. Skipper, G. Leisk, A. Saigal, D. Matson, and C. San Marchi, "Effect of internal hydrogen on fatigue strength of type 316 stainless steel," Proceedings of the 2008 International Hydrogen Conference, 7-10 September 2008, Moran WY. (Effects of Hydrogen on Materials, B.P. Somerday, P. Sofronis, R. Jones, editors, ASM International, Materials Park OH, 2009, pp. 139-146).

13 D. M. Matson, C. San Marchi, and A. Saigal, "Fatigue Behavior of Austenitic Stainless Steel Alloys Thermally Pre-Charged in Gaseous Hydrogen," International Hydrogen Conference, 9-12 September 2012, Moran, WY.

14 Y. Murakami, T. Kanezaki, and Y. Mine, "Hydrogen Effect against Hydrogen Embrittlement," *Metall. Mater. Trans. A Phys. Metall. Mater. Sci.*, vol. 41, no. 10, pp. 2548–2562, 2010.

15 SIERRA Solid Mechanics Team. Sierra/SolidMechanics 4.54 user's guide. SAND Report 2019-10735, Sandia National Laboratories, Albuquerque, NM and Livermore, CA, 2019.

16 J. T. Ostien, J. W. Foulk, A. Mota, and M. G. Veilleux, "A 10-node composite tetrahedral finite element for solid mechanics," *Int. J. Numer. Methods Eng.*, vol. 104, pp. 1145–1170, 2016.